Bioactive Materials 2 (2017) 1–9

Contents lists available at ScienceDirect

Bioactive Materials

journal homepage: http://www.keaipublishing.com/en/journals/bioactive-materials/

Effects of MgO modified β-TCP nanoparticles on the microstructure and properties of β-TCP/Mg-Zn-Zr composites

H.R. Zheng [a], Z. Li [a], C. You [a], D.B. Liu [a], M.F. Chen [a, b, *]

[a] School of Materials Science and Engineering, Tianjin University of Technology, China
[b] Tianjin Key Laboratory of Display Materials and Photoelectric Devices, China

ARTICLE INFO

Article history:
Received 20 February 2016
Received in revised form
28 December 2016
Accepted 29 December 2016
Available online 29 January 2017

Keywords:
MgO coated β-TCP nanoparticles
Magnesium matrix composites
Yield strength
Electrochemical corrosion
Cytocompatibility

ABSTRACT

The mechanical properties and corrosion resistance of magnesium alloy composites were improved by the addition of MgO surface modified tricalcium phosphate ceramic nanoparticles (m-β-TCP). Mg-3Zn-0.8Zr composites with unmodified (MZZT) and modified (MZZMT) nanoparticles were produced by high shear mixing technology. Effects of MgO m-β-TCP nanoparticles on the microstructure, mechanical properties, electrochemical corrosion properties and cytocompatibility of Mg-Zn-Zr/β-TCP composites were investigated. After hot extrusion deformation and dynamic recrystallization, the grain size of MZZMT was the half size of MZZT and the distribution of m-β-TCP particles in the matrix was more uniform than β-TCP particles. The yield tensile strength (YTS), ultimate tensile strength (UTS), and corrosion potential (Ecorr) of MZZMT were higher than MZZT; the corrosion current density (I_{corr}) of MZZMT was lower than MZZT. Cell proliferation of co-cultured MZZMT and MZZT composite samples were roughly the same and the cell number at each time point is higher for MZZMT than for MZZT samples.

1. Introduction

In order to meet clinical requirements, improvements in the mechanical properties and corrosion resistance of biodegradable magnesium (Mg) must be addressed. Alloys have been shown to raise the corrosion resistance and mechanical properties of the material [1], however few elements are biologically safe. There are many ways of preparing a surface coating of biomedical Mg alloy and these methods have been shown to effectively slow down the corrosion rate of the Mg alloy substrate at the early stages of implantation [2,3]. To prevent corrosion overtime, the bonding strength between the surface coating and Mg substrate must increase.

The addition of bioactive ceramic particles for reinforcement can improve the mechanical properties and corrosion resistance of biomedical Mg matrix composites, such as 20% n-ZnO/Mg [4], AZ91/FA [5] and β-TCP/Mg-Zn [6]. Sunil et al. [7] determined the strength, hardness, and corrosion resistance of Mg-HA composites prepared by spark plasma sintering (SPS) technology increased with the increase of ceramic particles, but particle agglomeration and the interface non-metallurgical state between the particles and the matrix led to poor plasticity, toughness, and comprehensive mechanical properties of the composites. Huan et al. [8] introduced bioactive glass (BG) into semi-solid ZK30 alloy under high pressure by a stir casting method to produce ZK30/BG composites with 0–20 wt% BG. Feng et al. [9] concluded the selection of ultrafine CPP particles (<750 nm) improved the mechanical properties of CPP/ZK60, demonstrating the yield tensile strength (YTS) and elongation of 5%CPP/ZK60 composites increased to 319.5 MPa and 30.5%, respectively.

Due to the poor wettability between biological active ceramic particles and the Mg alloy melt, ceramic particles are difficult to disperse evenly in a Mg composite matrix prepared by the stir casting method and the bonding interface may be affected by chemical reactions. Researchers have addressed this problem by forcing infiltration or surface modification of the ceramic particles. Ye et al. [10] modified HA with gelatin to prepare 1% HA/Mg-Zn-Zr composites by stir casting. Liu et al. [11] adopted a combination of high shear and adjustable, advanced melt shear technology to

* Corresponding author. School of Materials Science and Engineering, Tianjin University of Technology, China.
E-mail address: mfchentj@126.com (M.F. Chen).
Peer review under responsibility of KeAi Communications Co., Ltd.

http://dx.doi.org/10.1016/j.bioactmat.2016.12.004

prepare β-TCP/Mg-3Zn-Ca composites. This method improved the dispersion of β-TCP particle and reduced particles agglomeration. Further studies showed that Mg alloy had no effect on osteoblast toxicity and cell differentiation, suggesting Mg alloy could promote osteoblast differentiation, proliferation, growth, and adhesion by promoting the expression of related genes [12].

Our previous work showed the addition of tricalcium phosphate (β-TCP) or hydroxyapatite (HA) ceramic nanoparticles refine grain size and improve the mechanical properties and corrosion resistance of Mg-Zn-Zr alloy [13,14]. However, due to the poor wettability between ceramic nanoparticles and the Mg-Zn-Zr matrix, ceramic particle agglomeration was observed in the composite materials. In this paper, a semi-coherent boundary is formed between the ceramic nanoparticles and a Mg alloy matrix by modifying β-TCP with MgO in order to disperse the β-TCP in the Mg crystal core effectively. Using this method the problem of agglomeration was solved, the grain size of materials was refined, and the comprehensive performance of composite materials was raised. Effects of m-β-TCP nanoparticles on the microstructure, mechanical properties, electrochemical corrosion properties, and cytocompatibility of Mg-Zn-Zr/β-TCP composites were investigated.

2. Material and methods

2.1. Preparation of ceramic nanoparticles

β-TCP nanoparticles were obtained by slowly adding 100 ml aqueous $(NH_4)_2HPO_4$ to 100 mL aqueous $Ca(NO_3)_2 \cdot 4H_2O$ (1.5 Ca/P molar ratio) with continuous stirring. NaOH was used to adjust the pH to 8 and the solution was stirred for 3—5 h at room temperature. The solution was allowed to rest for 24 h prior to centrifugation. The product was dried (120 °C, 10 h), calcined (800 °C, 3 h) and ground to a fine powder.

MgO was coated on the surface of the β-TCP nanoparticles to prepare the modified β-TCP nanoparticles (m-β-TCP). β-TCP nanoparticles (2 g) were slowly added into a $Mg(NO_3)_2 \cdot 6H_2O$ aqueous solution (1.0 mol/L, 100 ml) with ultrasonic dispersion. An aqueous Na_2CO_3 solution (1.0 mol/L, 100 ml) was slowly added into the solution with continuous stirring at 40 °C. The solution was then allowed to sit (3 h), filtered, centrifuged, dried (80 °C) and calcined (600 °C, 3 h) to produce m-β-TCP.

2.2. Preparation of MZZMT and MZZT composites

Pure Mg (99.99%) ingot, Zn (99.99%) particles, Mg-Zr master alloy (with 30.89 wt% Zr), β-TCP and m-β-TCP nanoparticles were used as raw materials to prepare the Mg-3Zn-0.8Zr/1β-TCP (MZZT) and Mg-3Zn-0.8Zr/1m-β-TCP (MZZMT) composites. The raw materials were melted in an electric furnace equipped with a high shear, agitation device (Fig. 1, developed by BCAST, Brunel University London) under a complex protection atmosphere of 99.6% N_2 and 0.4% SF_6 for 10 min at 720 °C, and then the melt was molded in a metal pattern. This stirring method under high shear force reduces impurities and gases in the materials, allowing for even mixing. After a homogenizing annealing at 420 °C for 13 h, the cast ingots were skinned, warmed (350 °C, 2 h) and extruded by a YQ 32-315 extruder (Shangdong DaYin Industry Machine Co., Ltd) into Ø8mm bars with an extrusion ratio of 56.

2.3. Microstructure and phase analysis of composites

Nanoparticle morphology and size, and composite microstructure and grain size were observed by optical microscopy (OM, UTV0.5XC-3 OLYMPUS) and scanning electron microscopy (SEM, JOEL, JSM-6700F, Japan). Transmission electron microscopy (TEM, H-7000) was used to observe the second phase of the samples. Energy dispersive spectroscopy (EDS) was used to analyze composition. X-ray diffraction (XRD, D/max-2500, Japan) was used to examine phases with a diffraction angle range from 10° to 80° with 8°/min velocity.

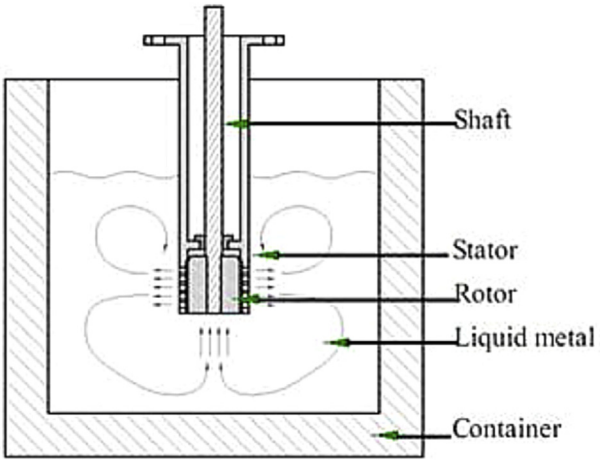

Fig. 1. Schematic diagram of the high shear, agitation device.

2.4. Mechanical properties of composites

A sclerometer (Japan HMV-2T) was used to determine the Vickers hardness of MZZT and MZZMT composites with a 9.8 N maximum load and 20 s loading time. At least 5 samples of each time point were tested to confirm reproducibility. Standard tensile samples of both composites were processed according to standard GB/T16865-1997. Tension tests were carried out on a WDW-100 electron universal testing machine with a strain rate of 0.5 mm/min. At each time point three samples were tested and the results were averaged.

2.5. Electrochemical testing

MZZT and MZZMT composites were processed into Ø8mm × 3 mm sample sizes and mechanically ground with SiC grit paper up to 3000. The electrochemical corrosion behavior of both composites were experimented in simulated body fluid (SBF) using an electrochemical workstation (Zennium, ZAHNER, Germany). SBF is composed of 3.273 g/L NaCl, 1.134 g/L $NaHCO_3$, 0.186 g/L KCl, 0.134 g/L $Na_2HPO_4 \cdot 7H_2O$, 0.152 g/L $MgCl_2 \cdot 6H_2O$, 0.184 g/L $CaCl_2 \cdot 2H_2O$, 0.036 g/L Na_2SO_4 and 3.029 g/L $(CH_2OH)_5CNH_2$ at pH 7.4 and 37 °C. A three-electrode system was set up for the electrochemical test. The counter electrode was made of graphite and the reference electrode was a saturated calomel electrode (SCE). 0.503 cm^2 of the working electrode (MZZT and MZZMT) was exposed to the SBF solution. Before each electrochemical test, the working electrode was immersed in SBF for 30 min to obtain a stable open circuit potential (OCP). The polarization scan was carried out at a scan rate of 1 mV/s. Three samples of each time point were tested to confirm reproducibility.

2.6. Cell culture experiments

For comparison, MZZT and MZZMT composites were used as a control and experimental group, respectively. Φ8 × 3 mm disks of the two composites were ground with increasing grades of SiC grit

paper up to 2400 and ultrasonically rinsed with distilled water and acetone sequentially. The disks were sterilized in 70% ethanol for 5 min and then washed three times in the SBF. The MZZT and MZZMT disks were then sterilized at 126 °C for 40 min under high pressure. Osteoblast cells from SD rats's skulls were used to perform the cell culture experiments. The cell culture medium consisted of DMEM containing 100 μg/ml penicillin and 100 μg/ml streptomycin. The cells were incubated in the medium at 37.4 °C in a humidified atmosphere with 5% CO_2 and were passaged routinely with the medium changes every second day during culture. The cells of harvested from the second passage were used in this study. The MZZT and MZZMT disks were placed in the bottom of 48-well plates and cell suspensions with a concentration of 0.5×10^4/ml were gently suspended on each the control and experimental group samples. The cells and composite samples were co-cultured in a well containing 3 ml cell suspensions for 1, 3, 5, and 7 days. The culture plates were incubated at 37.4 °C in a 5% CO_2 atmosphere without the replacement of the culture medium. After 1, 3, 5, and 7 days, three samples at the same time point were removed from the culture medium and washed twice with phosphate buffered saline (PBS) solution. The cells on the samples were detached in a 0.25% trypsin-EDTA solution and the number of cells on each sample was determined with a hemocytocounter to finished cells proliferation curve. Each data point was presented as means from three independent samples. SPSS 11.0 was used to evaluate the significant differences between cell growth on the samples of MZZT and MZZMT. The differences were considered significant at $p < 0.05$. A phase contrast microscope (TE2000-U, Nikon, Japan) was used to observe the morphology of the living cells on the edge of the samples in the wells.

3. Results and discussion

3.1. Characterization of m-β-TCP

XRD patterns of MgO, β-TCP and m-β-TCP are presented in Fig. 2 β-TCP and m-β-TCP characterized by XRD have same diffraction peaks at (1010), (0210), (1016), (4010), (0120) and (2020). The strongest diffraction peaks of MgO related to (200) and (220) appeared at $2\theta = 43°$ and 61°, respectively, were also observed in the XRD pattern of m-β-TCP, although the peaks are less intense. Therefore, the XRD pattern of m-β-TCP indicates the presence of both β-TCP and MgO, indicating the chemical reaction in m-β-TCP preparation did not change the crystal structure of β-TCP and a thin MgO layer was coated on the surface.

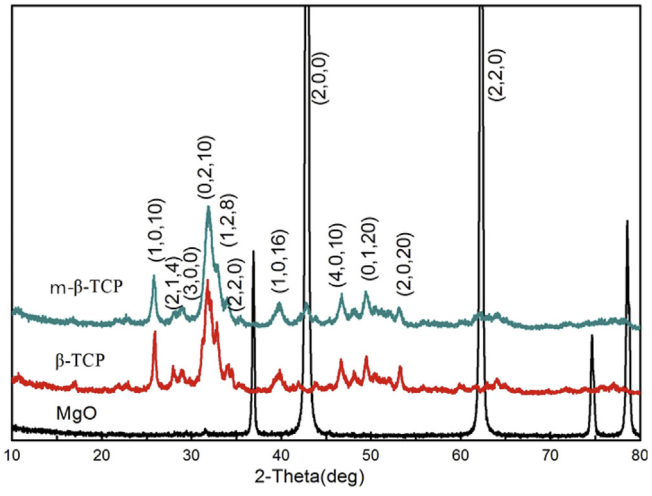

Fig. 2. XRD patterns of MgO, m-β-TCP, and β-TCP particles.

Fig. 3 shows the TEM images and EDS analysis of m-β-TCP (a, c) and β-TCP (b, d) nanoparticles. The m-β-TCP nanoparticles (25 nm) are larger and more dispersed than the β-TCP nanoparticles (18 nm). Both nanoparticles are spherical in shape. The m-β-TCP particles contain Mg, in addition to the elements of β-TCP (O, Ca, P). This result indicates a thin layer MgO was coated on the surface of the β-TCP particles, consistent with the XRD results shown in Fig. 2.

3.2. Microstructure and phase analysis of composites

Fig. 4 is the XRD patterns of the as-extruded MZZT and MZZMT composites. The diffraction peaks with the greatest intensity are Mg peaks. The β-TCP peaks at $2\theta = 20–25°$ and 45–55° are very weak because the addition of nanoparticles is only 1.0 wt%. However, the peaks prove the nanoparticles were added into Mg-Zn-Zr alloy by the high shear agitating method. In addition, MgO peaks are observed in the XRD pattern of the MZZMT composite.

Fig. 5 shows the microstructure of as-cast MZZMT and MZZT composites. Equiaxed grains are observed in both two composites. The addition of m-β-TCP nanoparticles favoured grain refinement and nanoparticle dispersion. The microstructure of MZZMT is uniform and the average grain size is about 9.2 μm. Tiny black punctate particles (m-β-TCP) are distributed in the intracrystalline and grain boundaries of MZZMT, and few nanoparticle agglomerations are observed (see arrows) (Fig. 5a). In contrast, Fig. 5b shows that the average grain size of MZZT is larger than MZZMT (16.5 μm) and the composite is nonuniform; the typical size of nanoparticle aggregates is 10 μm and they grew up to 20–30 μm (Fig. 5b). This indicates the β-TCP nanoparticles can be added into the Mg-Zn-Zr alloy matrix by the mandatory infiltration method, however the β-TCP nanoparticle agglomerates withstand mechanical stirring in smelting.

The OM and SEM images of the as-extruded MZZMT and MZZT composites are shown in Fig. 6. It can be observed that the microstructure of the two composites is more refined following hot extrusion. The average grain size of MZZMT (1.9 μm) composite is about half of MZZT (3.7 μm). Based on the microstructure of the as-cast composites, the fine and uniformly distributed m-β-TCP particles may inhibit the growth of recrystallization grains of Mg-Zn-Zr alloy. As shown in Fig. 6b, the agglomerated β-TCP nanoparticles distributed along the extrusion direction is strip-shaped, with nonuniform band structure about 10–20 μm long. This indicates the large hot plastic deformation does not prevent β-TCP particle aggregation. The variation between m-β-TCP and β-TCP nanoparticle distributions is clearly observed in SEM images of the as-extruded composites (Fig. 6c, d). The grain size of MZZMT is uniform and the aggregation of m-β-TCP particles is minimal (Fig. 6c). β-TCP particles aggregated in many areas of the MZZT composite and the grains become coarse in areas where no β-TCP particles are present (Fig. 6d).

Fig. 7 shows the TEM images and corresponding EDS analysis for the second phase and m-β-TCP particles of the as-extruded MZZMT composite. Two kinds of particles with different shapes, sizes and distributions are observed. The short rod-shaped particles distributed at the grain boundary of MZZMT composite are about 100–150 nm long (Fig. 7a) and corresponding EDS analysis (Fig. 7c) shows Mg and Zn are observed. These particles may be MgZn second phase combining with the analysis of MZZMT XRD pattern and Mg-Zn phase diagram. Small point-like particles are also observed in Fig. 7a, distributed uniformly in the matrix. Fig. 7b shows the amplification image of the small point-like particles. The shape of these particles is close to spherical and about 60–80 nm in diameter. These particles are composed of 2–3 small

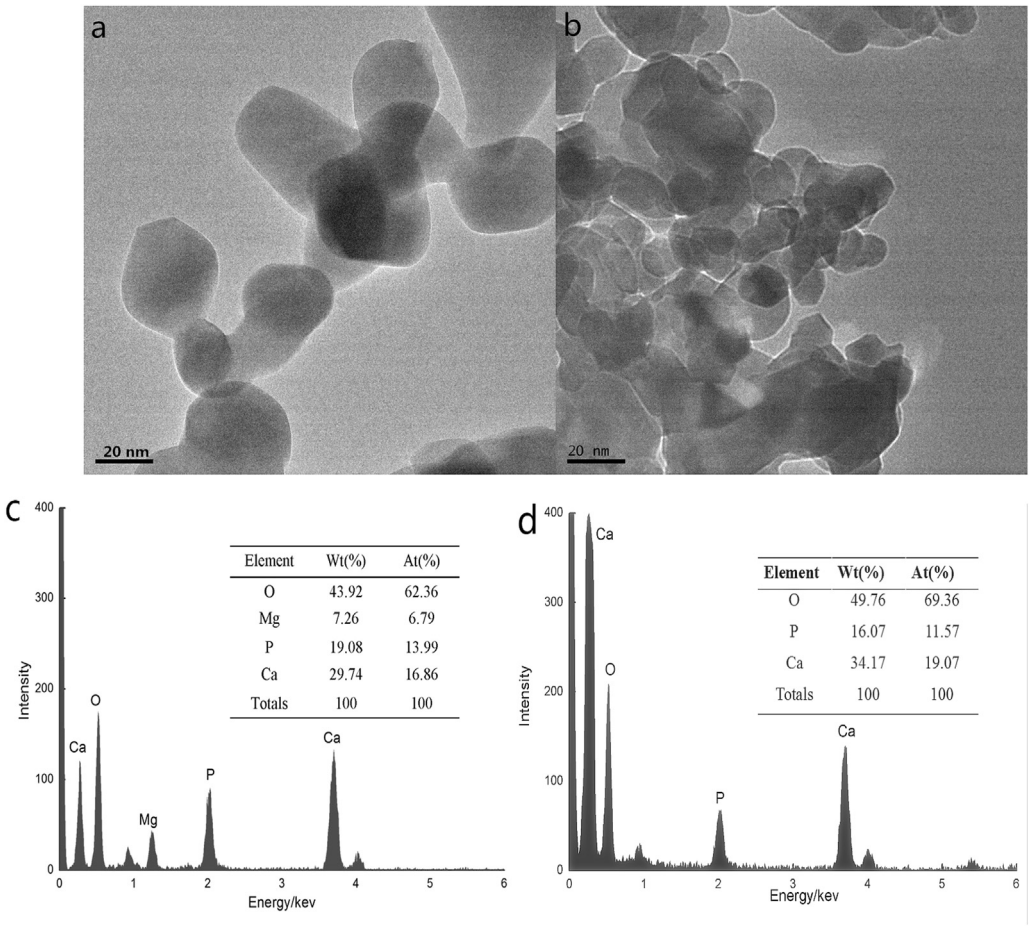

Fig. 3. TEM images and EDS analysis of (a, c) m-β-TCP and (b, d) β-TCP nanoparticles.

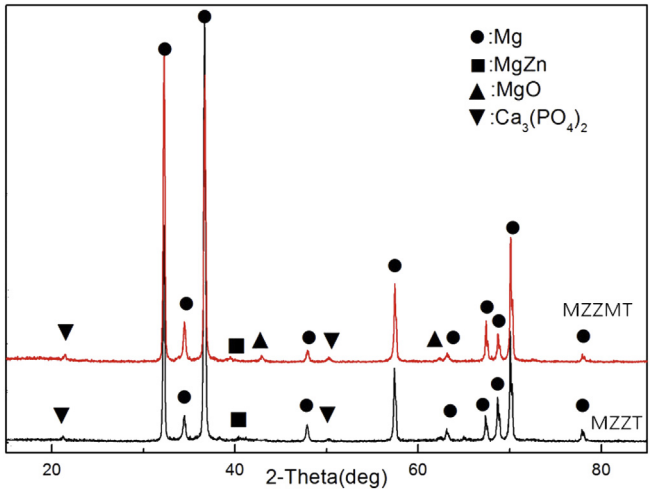

Fig. 4. XRD patterns of as-extruded MZZMT and MZZT composites.

particles about 20 nm in diameter. The outer layer of the spherical particle is covered by a gray layer. Corresponding EDS analysis (Fig. 7d) shows that the spherical particles consist of Ca, P, Mg and O elements. This indicates the spherical particles may be the β-TCP particles coated with MgO (m-β-TCP) distributed uniformly in MZZMT matrix.

3.3. Mechanical properties of composites

The Vickers hardness values of MZZMT and MZZT composites are shown in Fig. 8. The Vickers hardness of as-cast MZZMT composite is similar to as-cast MZZT. Due to the work hardening and dispersion hardening resulted by extrusion, the hardness value of the as-extruded composites increased significantly. The Vickers hardness value of as-extruded MZZMT composite is approximately 89 HV, slightly higher than that of MZZT composite (82 HV). Fig. 9 shows the average tensile properties of as-extruded MZZMT and MZZT composites. After hot extrusion, the YTS and UTS of MZZMT are 295.58 MPa and 346.11 MPa, respectively, which are 22.3% and 9.0% greater, respectively, than MZZT composites. The improvement to YTS of MZZMT composites may be the result of two scenarios. One, the grain size of MZZMT is merely half of MZZT, which greatly increases the quantity of grain boundaries in MZZMT. This can effectively prevent the movement of dislocation slip and improve the YTS. Additionally, the strength of a material is inversely proportional to the grain size according to the Hall-Petch formula: $\sigma = \sigma_0 + Ky \cdot d^{-1/2}$, where d is the grain size of the material and σ is the strength of the material; the higher the strength, the finer the grain size. Second, m-β-TCP dispersed uniformly in the MZZMT matrix, which can effectively pin dislocations. When stress is applied to the material, the deformation resistance of the material will increase and cause stress concentration. This may lead to the increase of the material strength and decrease the plasticity. As shown in Fig. 9, the elongation of MZZMT (10%) is similar to MZZT (11%). Compared with MZZT composite, the as-extruded MZZMT

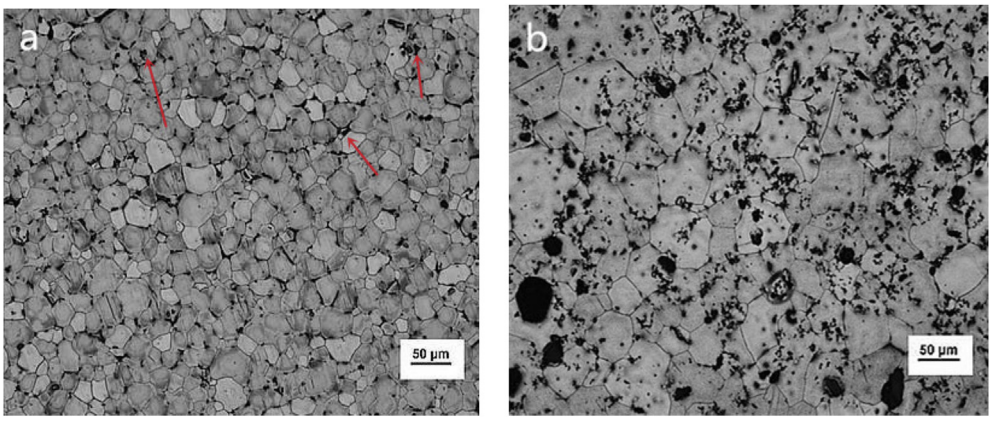

Fig. 5. OM images of as-cast (a) MZZMT and (b) MZZT composites.

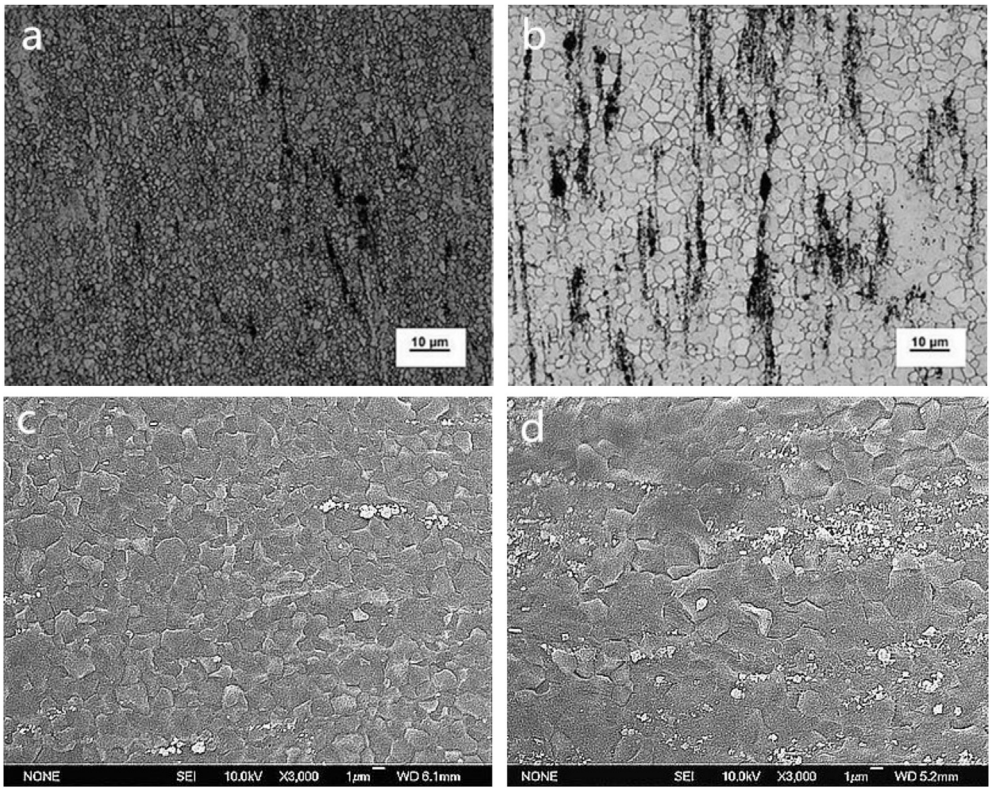

Fig. 6. OM images and SEM images of as-extruded (a,c) MZZMT and (b,d) MZZT composites.

composite exhibits mechanical properties with YTS (295.58 MPa), UTS (346.11 MPa) and elongation (10%).

3.4. The electrochemical properties of the composites

Fig. 10 shows the polarization curves of as-extruded MZZMT and MZZT composites in SBF at 37 °C. Table 1 shows the values of corrosion potentials (E_{corr}) and corrosion current density (I_{corr}) of the samples. For MZZMT composites, the E_{corr} is approximately 86 mV greater than MZZT, the I_{corr} is lower than MZZT. It is demonstrated that the modification of β-TCP can slow the corrosion rate and improve the corrosion resistance of composites.

Electrochemical impedance spectra (EIS) measurements of the as-extruded MZZMT and MZZT composites are shown in Fig. 11. The impedance diagram is composed of two capacitive arcs (located at high and intermediate frequencies) and an inductance arc (located at low frequencies). The diameter of the capacitive and inductance arcs are related to the corrosion resistance of the material. The larger the diameters of the capacitive and inductance arcs, the smaller the corrosion rate of the material. From Fig. 11, the diameter of the capacitive arc of the as-extruded MZZMT is larger than that of as-extruded MZZT, which indicates the charge transfer in MZZT is greater than MZZMT and the corrosion resistance of the MZZMT is greater than MZZT. Corresponding equivalent circuits for data fitting were developed and are shown in Fig. 12. R_S represents of solution resistance, R_t represents the charge transfer resistance and the corrosion resistance of samples raised with the value of R_t increasing, C_f representation of the double layer capacitance of the

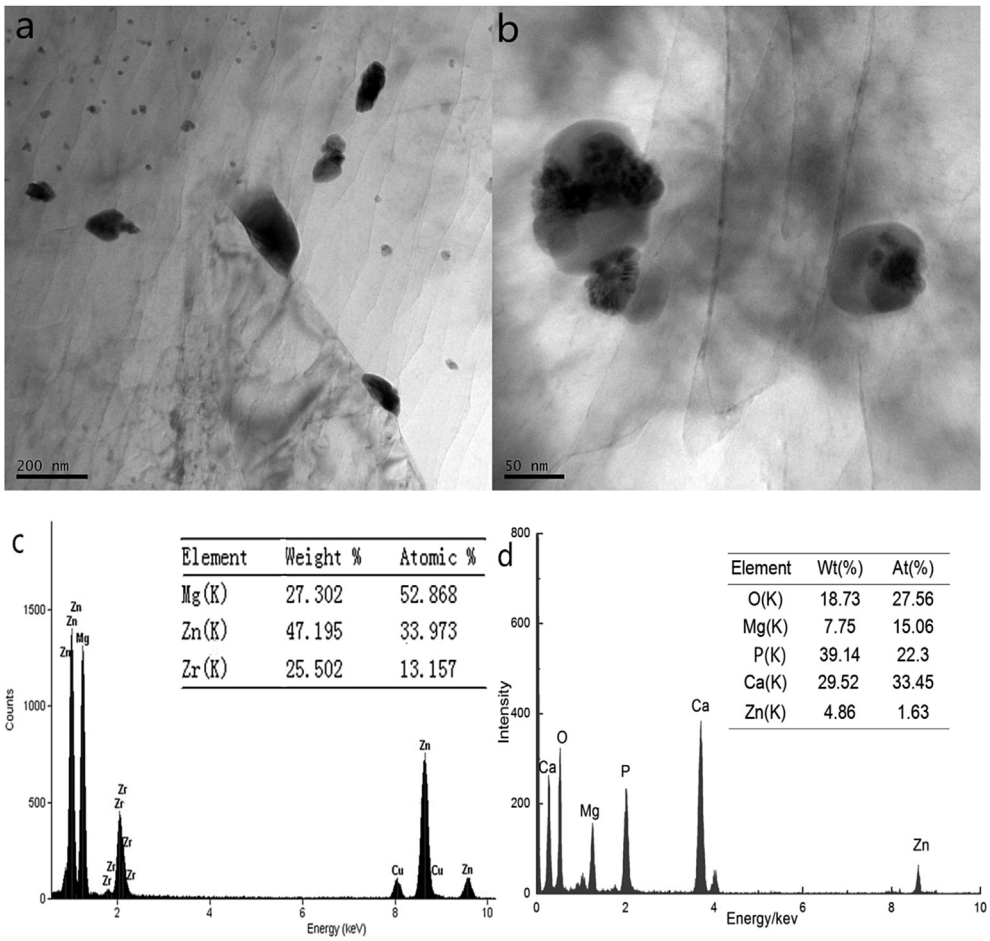

Fig. 7. TEM images and corresponding EDS analysis for second phase (c) and m-β-TCP particles (d) of the as-extruded MZZMT composite.

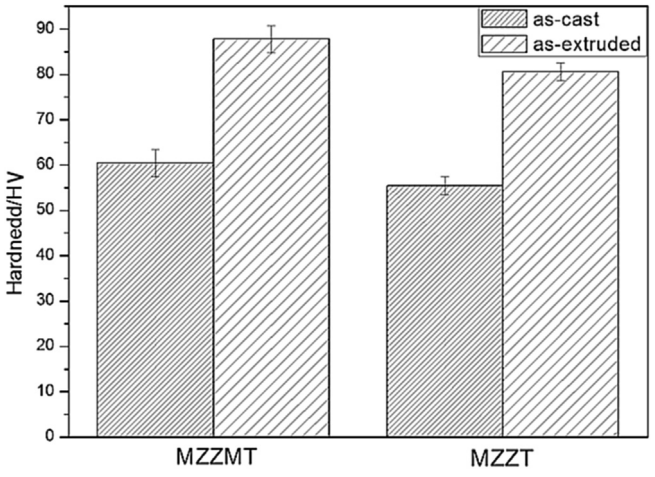

Fig. 8. Vickers hardness of composites.

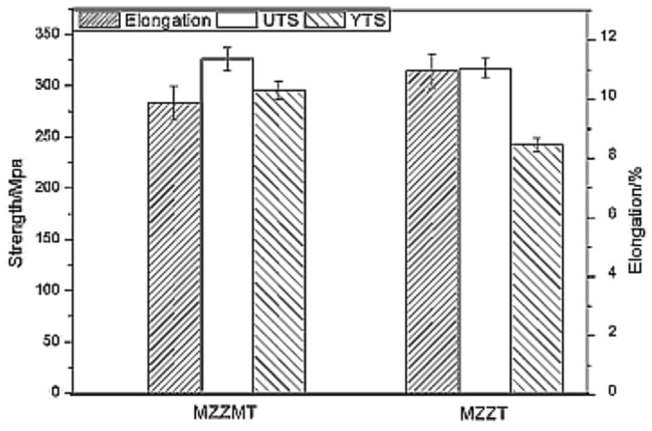

Fig. 9. Average tensile properties of as-extruded MZZMT and MZZT composites.

surface corrosion products and is a constant phase angle element, Q represents the equivalent element CPE, and n is the index of CPE. The fitted parameters of the impedance spectra are summarized in Table 2. Comparing the data in Table 2, the electrical parameters of the MZZMT and MZZT composites under the same conditions are significantly different. The charge transfer resistance (R_{t1}) of MZZMT is 3 times that of MZZT, and C_{f1} and Q values are 2 orders of magnitude higher than MZZT. This suggests in addition to the electrochemical corrosion resistance of the MZZMT, the density of the corrosion product layer is greater. This plays a role in protecting the Mg-Zn-Zr alloy matrix and consequently leads to more uniform corrosion on the MZZMT composite. The MZZT shows typical characteristics of non-uniform corrosion and may result in large areas of pitting corrosion and poor resistance.

The MgO coated β-TCP nanoparticles can distribute uniformly in the Mg-Zn-Zr alloy matrix, yielding the MZZMT composite with

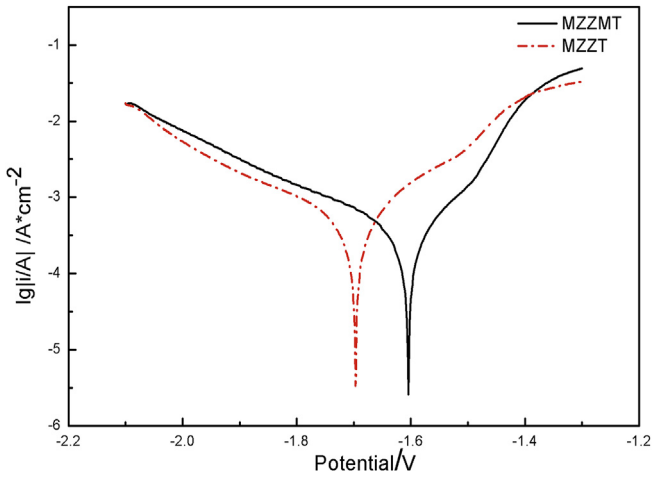

Fig. 10. Polarization curves of as-extruded MZZMT and MZZT composites in SBF at 37 °C.

Table 1
Electrochemical parameters of samples.

Sample	E_{corr} (V)	$I_{corr}(10^{-4}$ A $cm^{-2})$
MZZMT	−1.607 ± 0.03	2.009 ± 0.9
MZZT	−1.693 ± 0.04	3.084 ± 0.6

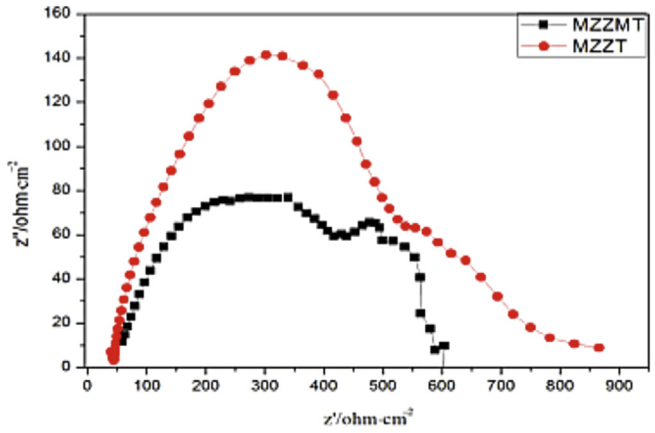

Fig. 11. EIS measurements of as-extruded MZZMT and MZZT composites.

finer grains and a more uniform microstructure. Therefore, a dense corrosion layer forming on the MZZMT composite raises the charge transfer resistance and improves the homogeneity of the corrosion layer. The resulting corrosion resistance of the as-extruded MZZMT is thus higher than that of the as-extrusion MZZT.

3.5. Analysis of cell proliferation

MZZMT and MZZT composite samples were co-cultured with osteoblast cells for up to five days and the cell morphology around the composite samples in culture plates are shown in Fig. 13. After co-culture for one day cells grew around MZZMT, some attached to the boundary of specimen and the shape of most cells is fusiform or polygon (Fig. 13a). In the control group, cell attachment at the edge of the MZZT composite is rare and corrosion at the boundary is observed by black masses (Fig. 13b). After three days (Fig. 13c, d) the number of cells in the two groups increased and more cells are attached to MZZMT. After five days (Fig. 13e, f), the cells co-cultured with MZZMT grew dense with regularity, increasing in quantity and retaining the fusiform shape, while change in cell growth is not obvious in the MZZT co-culture control group. Signs of corrosion in the sample edge are observed in both samples, however corrosion is less prevalent in the MZZMT co-culture samples, indicative of greater corrosion resistance in MZZMT.

The cell growth curves of the samples are shown in Fig. 14. As expected, the number of cells in the two groups increased with the extension of incubation time. Although the trend of cell growth is similar between the two groups, the number of cells in the experimental group is higher than the control group. Cells on the surface of the samples decreased after co-culture for 7 days due to competitive inhibition of cell growth. From a statistical analysis, the quantity of cell on MZZMT and MZZT are different ($p < 0.05$) for 3 and 5 day incubation times, indicating the cytocompatibility of MZZMT is better than the control group sample MZZT. When materials and cells are co-cultured, the growth environment is controlled by conflicting factors. Hydroxyl ions (OH^-) and hydrogen (H_2) are released in the degradation process of Mg-based materials. OH^- can increase the alkalinity of the nutrient solution and inhibit cell reproduction and growth, and H_2 disrupts adherent grow of cells. Whereas, Mg^{2+} released in the degradation process of Mg-based materials can promote the proliferation, differentiation, growth, and adhesion of osteoblast cells by enhancing the expression of related genes. Also, β-TCP nanoparticles in the composites promote cell growth. The poor corrosion resistance of MZZT accelerates the adverse impact of OH^- and H_2 on growth of cells. As a result, the quantity of cells for MZZT co-culture samples is less than MZZMT in every time points. In MZZMT composites, uniformly distributed m-β-TCP improves the corrosion resistance of the matrix alloy by grain refinement. The combined effect of both m-β-TCP and Mg^{2+} released in the degradation process of materials improves the function and metabolic activity of the osteoblast cells and is a benefit for the attachment and proliferation of cells on the sample surface.

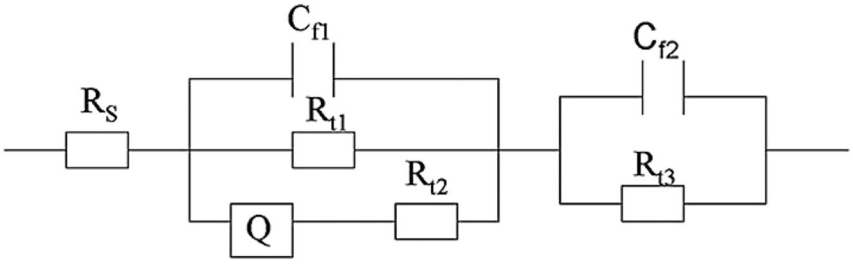

Fig. 12. Equivalent circuit of EIS plots for MZZMT and MZZT composites.

Table 2
Fitting results of EIS plots for MZZMT and MZZT composites.

Sample	R_s (Ωcm^2)	C_{f1} ($10^{-8}Fcm^{-2}$)	R_{t1} (Ωcm^2)	Q ($\Omega^{-1}s^n cm^2$)	n	R_{t2} (Ωcm^2)	C_{f2} (Fcm^{-2})	R_{t3} (Ωcm^2)
MZZMT	21.44	126.1	69.13	224.4×10^{-5}	0.8413	109.4	77.62×10^{-5}	89.79
MZZT	15.53	4.651	22.16	7.868×10^{-5}	0.5687	24.5	1.784×10^{-5}	53.32

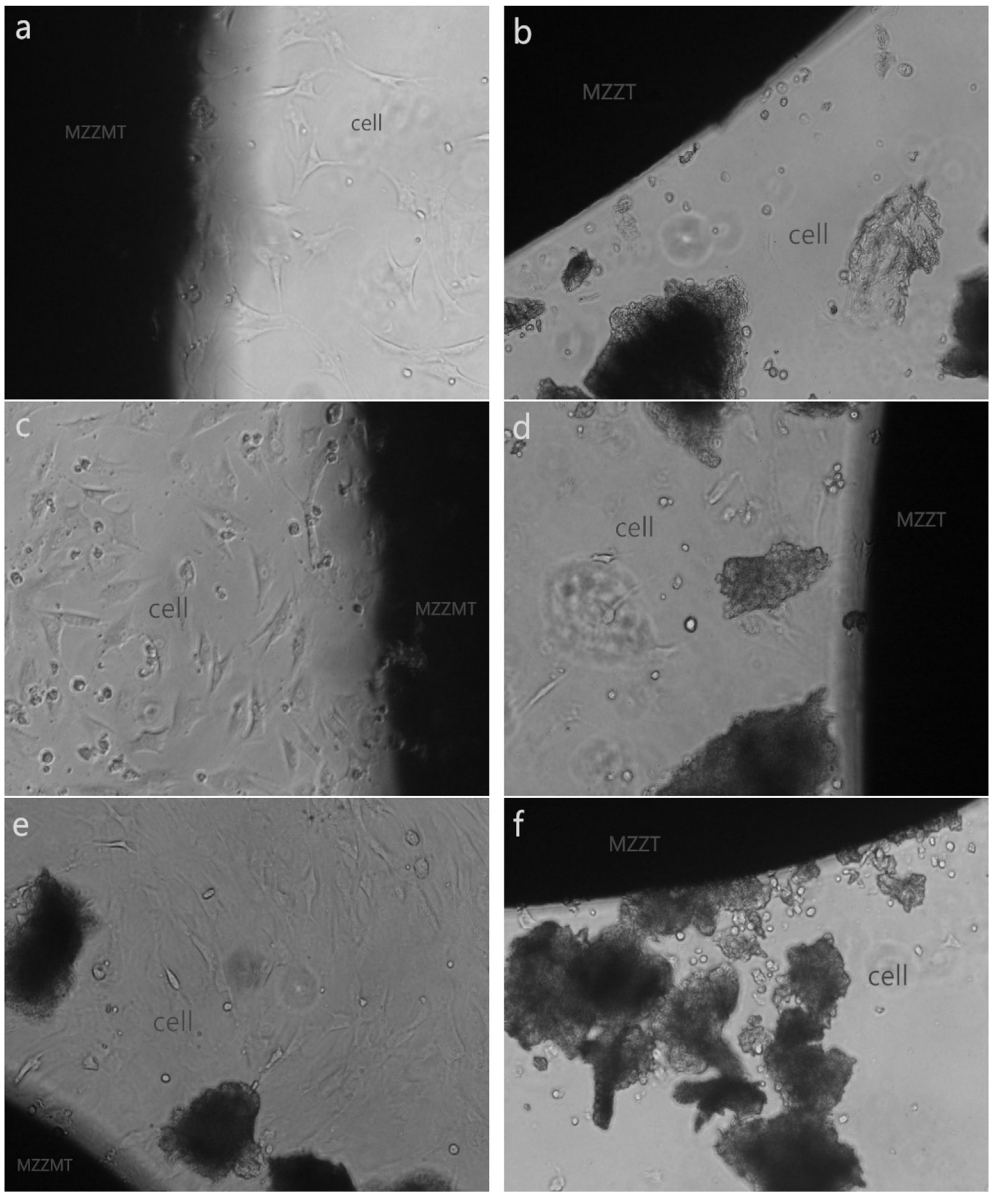

Fig. 13. Cell morphology of samples following co-culture for 1 day (a,b), 3 days (c,d), and 5 days (e,f).

4. Conclusions

MgO particles were successfully coated on the surface of β-TCP nanoparticles using a chemical precipitation method. The newly synthesized m-β-TCP particles are larger than β-TCP nanoparticles and Mg-3Zn-0.8Zr composite dispersion improved. Compared with the as-cast MZZT composite, the grain size of the as-cast MZZMT is refined to 9.2 μm. The distribution of the grain size and m-β-TCP particles are more uniform. In the hot extrusion process, the microstructure of the composites improved due to plastic deformation, dynamic recovery, and recrystallization. The grain size of the as-extruded MZZMT is half of the as-extrusion MZZT. The m-β-TCP nanoparticles evenly distributed in the Mg-Zn-Zr alloy matrix, while the β-TCP has significant local agglomeration. After hot extrusion, the YTS and UTS of the MZZMT reaches 295.58 MPa and 346.11 MPa, respectively, which increased by 22.3% and 9.0%, respectively, compared with MZZT. The E_{corr} of the as-extruded MZZMT composite increases 86 mV compared with MZZT, and the I_{corr} is lower than MZZT composite. The addition of m-β-TCP to the Mg alloy has good cell compatibility, which is related to the

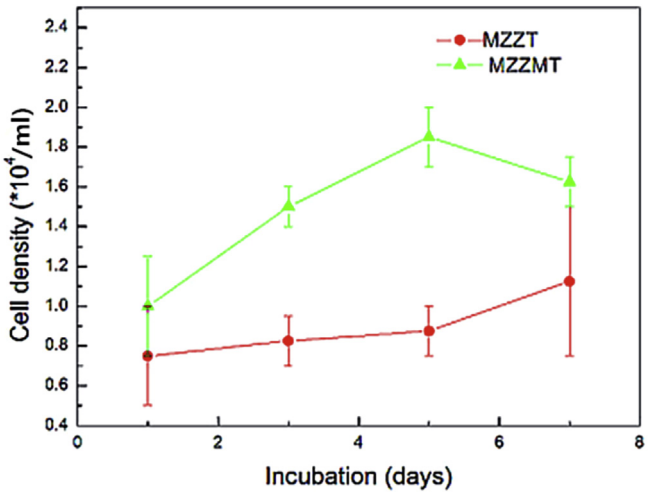

Fig. 14. Cell growth curves of the MZZMT and MZZT samples composites.

slower degradation rate of MZZMT compared to MZZT. The cytocompatibility of two composites can be ranked as follows: MZZMT > MZZT.

Acknowledgements

The authors acknowledge the financial support for this work from the National Nature Science Foundation of China (No. 51371126 and No. 51271131), Science and Technology supporting program in Tianjin (No.14ZCZDGX00007), Major science and technology projects in Tianjin (No. 15ZXQXSY00080).

Appendix A. Supplementary data

Supplementary data related to this article can be found at http://dx.doi.org/10.1016/j.bioactmat.2016.12.004.

References

[1] Y.F. Zheng, X.N. Gu, F. Witte, Biodegradable metals, Mater. Sci. Eng. R 77 (2014) 1–34.
[2] A. Jankovic, S. Erakovic, M. Mitric, et al., Bioactive hydroxyapatite/graphene composite coating and its corrosion stability in simulated body fluid, J. Alloys Compd. 624 (2015) 148–157.
[3] H.Y. Xia, B.P. Zhang, C.X. Lu, et al., Improving the corrosion resistance of Mg-4.0Zn-0.2Ca alloy by micro-arc oxidation, Mater. Sci. Eng. C 33 (2013) 5044–5050.
[4] T. Lei, W. Tang, S. Cai, et al., On the corrosion behaviour of newly developed biodegradable Mg-based metal matrix composites produced by in situ reaction, Corros. Sci. 54 (2012) 270–277.
[5] M. Razavi, M.H. Fathi, M. Meratian, Mechanical properties and bio-corrosion evaluation of biodegradable AZ91-FA nanocomposites for biomedical applications, Mater. Sci. Eng. A 527 (2010) 6938–6944.
[6] K. Yu, L.J. Chen, J. Zhao, et al., In vitro corrosion behavior and in vivo biodegradation of biomedical β-$Ca_3(PO_4)_2$/Mg-Zn composites, Acta Biomater. 8.7 (2012) 2845–2855.
[7] S.B. Ratna, C. Ganapathy, T.S. Sampath Kumar, et al., Processing and mechanical behavior of lamellar structured degradable magnesium–hydroxyapatite implants, J. Mech. Behav. Biomed. 40 (2014) 178–189.
[8] Z.G. Huan, M.A. Leeflang, J. Zhou, et al., ZK30-bioactive glass composites for orthopedic applications: a comparative study on fabrication method and characteristics, Mater. Sci. Eng. B 176 (2011) 1644–1652.
[9] A. Feng, Y. Han, Mechanical and in vitro degradation behavior of ultrafine calcium polyphosphate reinforced magnesium-alloy composites, Mater. Des. 32 (2011) 2813–2820.
[10] X. Ye, M. Chen, M. Yang, et al., In vitro corrosion resistance and cytocompatibility of nano-hydroxyapatite reinforced Mg–Zn–Zr composites, J. Mater. Sci. Mater. Med. 21 (2010) 1321–1328.
[11] D. Liu, Y. Zuo, W. Meng, et al., Fabrication of biodegradable nano-sized β-TCP/Mg composite by a novel melt shearing technology, Mater. Sci. Eng. C 32 (2012) 1253–1258.
[12] A. Loos, R. Rohde, A. Haverich, et al., In vitro and in vivo biocompatibility testing of absorbable metal stents, Macromol. Symp. 253 (2007) 103–108.
[13] S.Y. He, Y. Sun, M.F. Chen, et al., Microstructure and properties of biodegradable β-TCP reinforced Mg-Zn-Zr composites, T. Nonferr. Metal. Soc. China 21.4 (2011) 814–819.
[14] X. Ye, M. Chen, M. Yang, et al., In vitro corrosion resistance and cytocompatibility of nano-hydroxyapatite reinforced Mg-Zn-Zr composites, J. Mater. Sci. Mater. Med. 21 (4) (2010) 1321–1328.